Tunable Localized Charge Transfer Excitons in a Mixed Dimensional van der Waals Heterostructure

Mahfujur Rahaman[1], Emanuele Marino[2,3], Alan G. Joly[4], Seunguk Song[1], Zhiqiao Jiang[2,4], Brian T. O'Callahan[4], Daniel J. Rosen[5], Kiyoung Jo[1], Gwangwoo Kim,[1] Patrick Z. El-Khoury[4], Christopher B. Murray[2,5], and Deep Jariwala[1]

[1]Department of Electrical and Systems Engineering, University of Pennsylvania, PA 19104, USA

[2]Department of Chemistry, University of Pennsylvania, PA 19104, USA

[3]Dipartimento di Fisica e Chimica, Università degli Studi di Palermo, Via Archirafi 36, 90123 Palermo, Italy

[4] Physical and Chemical Sciences Division, Pacific Northwest National Laboratory, Richland, WA 99352, USA

[5] Department of Materials Science and Engineering, University of Pennsylvania, PA 19104, USA

Abstract

Observation of interlayer, charge-transfer (CT) excitons in van der Waals heterostructures (vdWHs) based on 2D-2D systems has been well investigated. While conceptually interesting, these charge transfer excitons are highly delocalized and spatially localizing them requires twisting layers at very specific angles. This issue of localizing the CT excitons can be overcome via making mixed dimensional vdWHs (MDHs) where one of the components is a spatially quantum confined medium. Here, we demonstrate the formation of CT excitons in a 2D/quasi-2D system comprising $MoSe_2$ and WSe_2 monolayers and CdSe/CdS based core/shell nanoplates (NPLs). Spectral signatures of CT excitons in our MDHs were resolved locally at the 2D/single-NPL heterointerface using tip-enhanced photoluminescence (TEPL) at room temperature. By varying both the 2D material, the shell thickness of the NPLs, and applying out-of-plane electric field, the exciton resonance energy was tuned by up to 120 meV. Our finding is a significant step towards the realization of highly tunable MDHs with novel excitonic properties.

Introduction

Interlayer excitons (ILXs) are composed of Coulomb bound electron and hole (*e-h*) pairs confined in two different spatially separated quantum wells that are coupled together electronically. Owing to large spatial separation of *e-h* pairs, ILXs possess much longer lifetimes (1 – 3 order of magnitude higher) than the direct excitons of individual QWs[1,2]. This allows ILXs to be subsequently explored for strongly correlated condensed matter phenomena such as Bose-Einstein condensates as well as in excitonic, and photonic devices[3,4]. Experimental observation of ILXs was first reported in coupled GaAs/AlGaAs QWs and later in various III-V and II-VI QW heterostructures[5]. However, the very small exciton binding energy (few meV) of conventional 3D semiconductor QW heterostructures limited the progress of this field to cryogenic measurements[6].

The recent emergence of both structural as well as electronic variety in 2D materials has opened new opportunities to study ILXs. Van der Waals heterostructures (vdWHs) composed of several combinations of distinct 2D materials, especially transition metal dichalcogenides (TMDCs), allow the formation of ILXs with remarkably high binding energies (100 – 350 meV)[7]. Hence, it is possible to observe ILXs in such vdWHs at room temperature (RT), which has made it an intense research topic in recent years[8,9]. ILXs formed in 2D/2D systems are generally delocalized in the 2D plane and require a specific twisting angle between the participating monolayers to create localized excitons in the 2D landscape[10,11]. As a result, forming localized ILXs in a twisted heterobilayer (HB) can function as quantum dot-like (QD) confined potentials which unlock exciting opportunities towards high-performance semiconducting lasers, single photon emitters, entangled photon sources, and tunable exotic quantum phases of matter[4,12,13]. Despite the recent great efforts of spatially confining ILX in HBs with precisely controlled angles, imperfection in crystals, challenges with sophisticated sample preparation, and the repulsive interaction between the confined excitons keep the localization process far from ideal both in terms of energy (spectral lines) and spatial extent[14,15].

52   In this context, mixed dimensional heterostructures (MDH) composed of 2D materials on

53   one side and 0D or spatially confined materials on the other side can be an attractive option for

54   the creation of localized ILXs. Due to the van der Waals nature of the interface formed between

55   2D and 0D or spatially confined materials, MDHs favor similar charge transport phenomena

56   analogous to all-2D vdWHs, when formed with type-II band alignment[16–19]. Therefore, it is

57   predicted that MDHs can also emit ILX-like excitons, which are known as hybrid or charge

58   transfer (CT) excitons[20,21]. Additionally, reduced dimensionality of one of the materials can

59   introduce arbitrary spatial and energy confinement as well as additional degrees of freedom at

60   the interfaces to tune electronic properties of MDHs[20]. Hence, in contrast to delocalized ILXs in

61   all-2D vdWHs, CT excitons formed in MDH heterointerfaces should be localized along the reduced

62   dimensional materials in the out-of-plane direction. This leads to the possibility of investigating

63   and manipulating localized CT excitons in the 2D landscape of the respective MDH. Moreover,

64   owing to the differences in the density of states and dielectric screening environments on either

65   side of the heterostructure, the mechanism of the CT exciton formation and the consequent

66   parameters that can control it may be fundamentally different compared to all-2D systems[22].

67   Importantly, the constraints on localization of ILX-like excitons in terms of energy and spatially

68   are eliminated in the case of MDHs. Therefore, MDHs present a new platform to investigate

69   charge-transfer physics and subsequent exciton formation in MDHs, and will have a broader

70   technological impact on many device applications[23,24].

71   In this work, we report on the observation of CT excitons in MDHs composed of 2D

72   transition metal dichalcogenides (TMDCs) and colloidal semiconducting $CdSe/Cd_xSZn_{1-x}S$

73   core/shell nanoplates (NPLs). Even though these nanoplates are colloidal semiconducting

74   nanocrystals, their density of states more resemble a step-like quasicontinuum similar to a 2D

75   electronic system[25]. Therefore, these nanoplates are known as quasi-2D (Q2D) systems. We adopt

76   tip- enhanced photoluminescence (TEPL) nano-spectroscopy to resolve the spectral signature of

77   CT excitons from a single NPL/2D heterointerface. Taking advantage of large tunability of the

78   band structure as a function of shell thickness of $CdSe/Cd_xSZn_{1-x}S$ based core/shell NPLs and

79 combining them with monolayer MoSe$_2$ and WSe$_2$ we are able to tune the CT exciton up to 120

80 meV. Our work presents primary experimental evidence of the presence of CT excitons with large

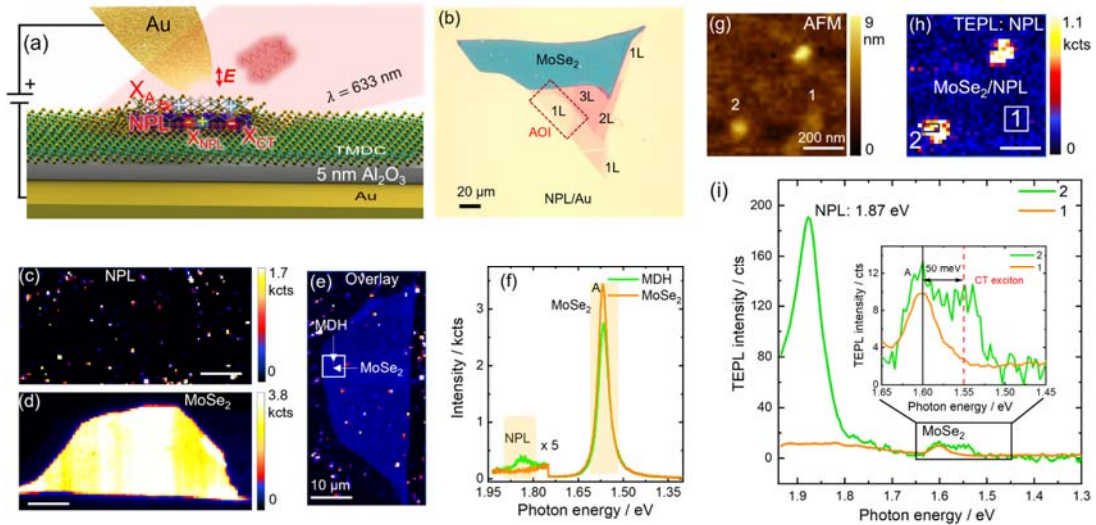81 tunability in a MDH system.

Figure 1. Micro- and nano-optical characterization of CT excitons in MDHs. (a) Schematic representation of TEPL measurements of the MDHs containing TMDC monolayers (MoSe$_2$ and WSe$_2$) on top of CdSe/CdS$_x$Zn$_{1-x}$S core/shell NPLs on an Au (or Al$_2$O$_3$/Au) substrate. For the electric field dependent study an out-of-plane bias was applied through the tip and metal substrate. (b) Optical image of one representative MDH device investigated in this work. Area of interest (AOI) is outlined by a dashed rectangle. (c), (d) Far-field PL intensity map of NPL and MoSe$_2$ acquired for the AOI region. (e) PL intensity overlay image using (c) and (d) showing the MDH interface formation on a MoSe$_2$ monolayer. Scale bar is 10 μm. (f) two representative far-field PL spectra of MoSe$_2$ and MDH acquired from two nearby pixels as marked in the overlay image. NPL Spectral regions are multiplied by 5 for better visibility. Orange shades are the spectral regions for which PL maps were created for NPL and MoSe$_2$ respectively. (g), (h) AFM topography and corresponding TEPL intensity map of NPLs on monolayer MoSe$_2$ acquired simultaneously. (i) Two representative TEPL spectra averaged over the rectangle areas marked by 1 and 2 in the TEPL image.

82 **Results and Discussions**

83 Fig. 1a presents a schematic of the TEPL configuration used to characterize MDHs in this study.

84 The MDHs containing monolayer MoSe$_2$ (or monolayer WSe$_2$) and CdSe/Cd$_x$SZn$_{1-x}$S core/shell

85 NPLs have three different excitons: two in-plane excitons from the TMDCs and NPL respectively

86 and one out-of-plane CT exciton across the MDH interface as schematically presented. A gold tip

87 was used to excite the plasmonic field underneath using 633 nm excitation. Fig. 1b shows an

88 optical image of one of the representative MDH samples studied in this work. Details of the MDH

89 device fabrication, NPLs synthesis and characterization can be found in the method section and

90 the supplementary information section I. Far-field PL intensity maps created for NPLs and $MoSe_2$

91 and their overlay image for the area of interest (AOI) region marked in the optical image (Fig. 1b)

92 are shown in Fig. 1c-e respectively. The representative far-field-PL spectra for both MDH and

93 monolayer $MoSe_2$ are displayed in Fig. 1f. The orange shades are the spectral region for which the

94 NPL and $MoSe_2$ PL maps were created in Fig. 1c, d. As can be seen in Fig. 1e, the MDHs form at

95 multiple locations between NPLs and $MoSe_2$. Wherever they form an electronic contact, MDHs

96 emit CT excitons as revealed by TEPL. However, it is challenging to resolve CT excitons in the far-

97 field-PL configuration due to the close proximity of this peak to the A exciton of $MoSe_2$ and the

98 large probing cross-section of the far-field PL geometry (~ 0.2 μm^2) compared to a very small CT

99 exciton emitting area (limited by the spatial extent of NPLs: 6×10^{-4} μm^2). These factors ultimately,

100 lead to very weak CT exciton signals in the far-field PL spectroscopy geometry, (see

101 supplementary information section II for more details).

102 The situation can be changed by introducing TEPL, which excites/emits signal locally under

103 the tip apex with high spatial resolution. Fig. 1g,h show atomic force microscope (AFM) and

104 corresponding TEPL intensity images of NPLs on $MoSe_2$ respectively. Our sub-20 nm spatial

105 resolution was enough to resolve CT exciton from a single NPL/2D MDH interface (see

106 supplementary information Fig. SI-2ii). Despite the excellent sensitivity of TEPL (both

107 enhancement and spatial resolution), the large extent of the 2D plane can still introduce an
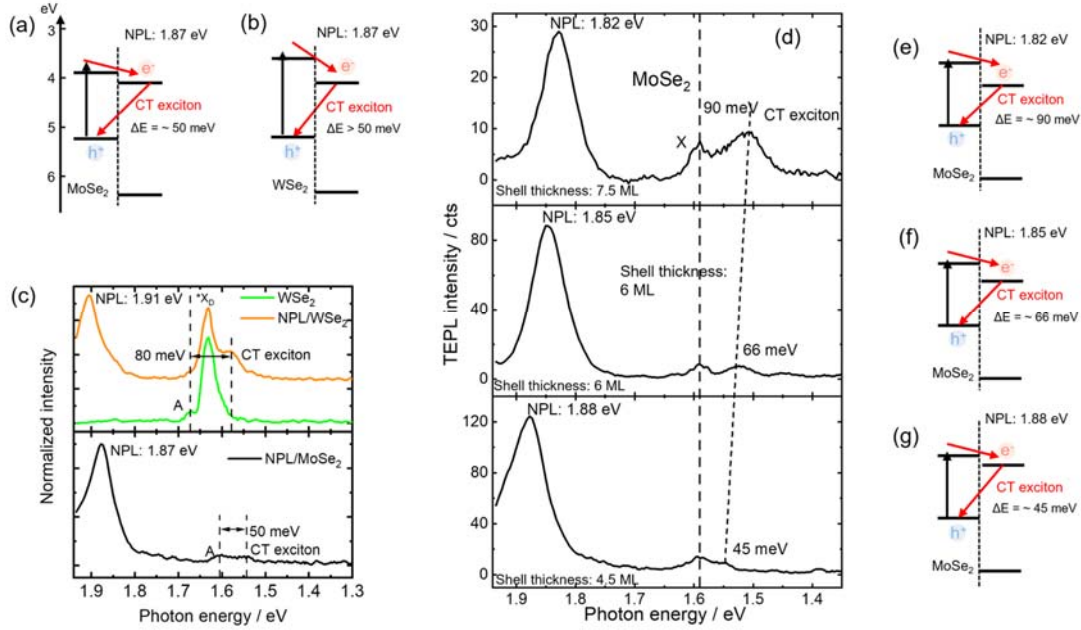
Figure 2. Band alignment engineered tunability of CT excitons in MDH. (a), (b) Band alignment diagrams at 2D/Q2D interfaces studied in this work. Values are taken from the refs[26,27]. (c) TEPL spectra acquired for the WSe$_2$/NPL system. For comparison TEPL spectra of bare WSe$_2$ and MoSe$_2$/NPL of Fig. 1i are also plotted. (d) Tuning of CT excitons via NPL shell thickness variation for NPL/MoSe$_2$ system. (e) – (g) Schematic illustration of band alignment for CT exciton tuning via NPL shell thicknesses.

108 additional challenge in resolving spectral features from the MDH areas since the TEPL signal

109 needs to overcome a large far-field background (see supplementary information section III).

110 Hence, all the TEPL measurements were treated with far-field background subtraction to resolve

111 the CT excitons in MDHs clearly. Two representative TEPL spectra, one averaged from the NPL

112 region (black rectangle area) and the other from MoSe$_2$ (white rectangle area) marked in Fig. 1h

113 can be seen in Fig. 1i. It is Important to note that MDH spectrum is averaged over 4 pixels (pixel

114 size is 20x20 nm) corresponding to two NPLs (see table S1 in the supplementary section I)

115 making it noisier than the MoSe$_2$ spectra (averaged over 42 pixels). We can clearly observe three

116 PL features in the MDH spectrum in Fig. 1i. Among them, two main excitonic features, NPL PL and

117 MoSe$_2$ A exciton peak are observed at 1.87 eV and 1.60 eV respectively. The third PL peak is

118 observed 50 meV below the MoSe$_2$ A exciton peak in the MDH spectra. We assigned this peak as

119   the CT exciton via *e-h* recombination from NPL to $MoSe_2$ and will provide further evidence to our

120   claim in the following sections.

121   To understand the CT mechanism and the consequent exciton formation at the MDH

122   interface under investigation, we analyse the band diagram using the band values available in

123   the literature for both the semiconductors in the MDH[26,27]. The band alignment presented in Fig.

124   2a predicts photoexcited electron transfer from $MoSe_2$ to NPLs and then *e-h* recombination from

125   NPL CB to $MoSe_2$ VB, which can be observed as CT exciton in our system. We followed two

126   approaches to confirm the origin of this emission peak. The first one is via changing the 2D

127   material as shown in the band alignment diagram of Fig. 2b. Since the band edges of monolayer

128   WSe_2 move higher in energy compared to monolayer $MoSe_2$, it should create CT excitons of

129   smaller energy (larger energy offset) when paired with NPLs of the same bandgap. TEPL spectra

130   acquired for NPL/WSe_2 system presented in Fig. 2c demonstrates this hypothesis. For

131   comparison, TEPL spectra of bare WSe_2 acquired from a nearby area and the NPL/$MoSe_2$

132   spectrum of Fig. 2d is also plotted together. The main excitonic feature (bright exciton, A) of WSe_2

133   is observed at 1.66 eV as a shoulder to the strong dark exciton, X_D around 1.62 eV in our TEPL

134   spectra. Even though dark excitons in WSe_2 are not permitted in far-field geometry, they can be

135   observed in TEPL at RT due to the strong coupling between the out-of-plane exciton dipole

136   moment and the plasmonic field in the nano-cavity[28,29]. Nevertheless, most importantly, the CT

137   exciton peak can be observed at 80 meV below the WSe_2 A exciton. Hence, from Fig. 2c, it is clear

138   that the NPL/WSe_2 interface creates CT excitons with larger band offset than the NPL/$MoSe_2$

139   interface. Note that the slight deviation of the bandgap of NPL is due to thickness variation (a

140   consequence of NPL synthesis process) of the NPL.

141   As a second approach, we also test the possibility of tuning the CT exciton energy via changing

142   the NPL shell thickness. As predicted in the literature, quasi-type II CdSe/CdS based core/shell

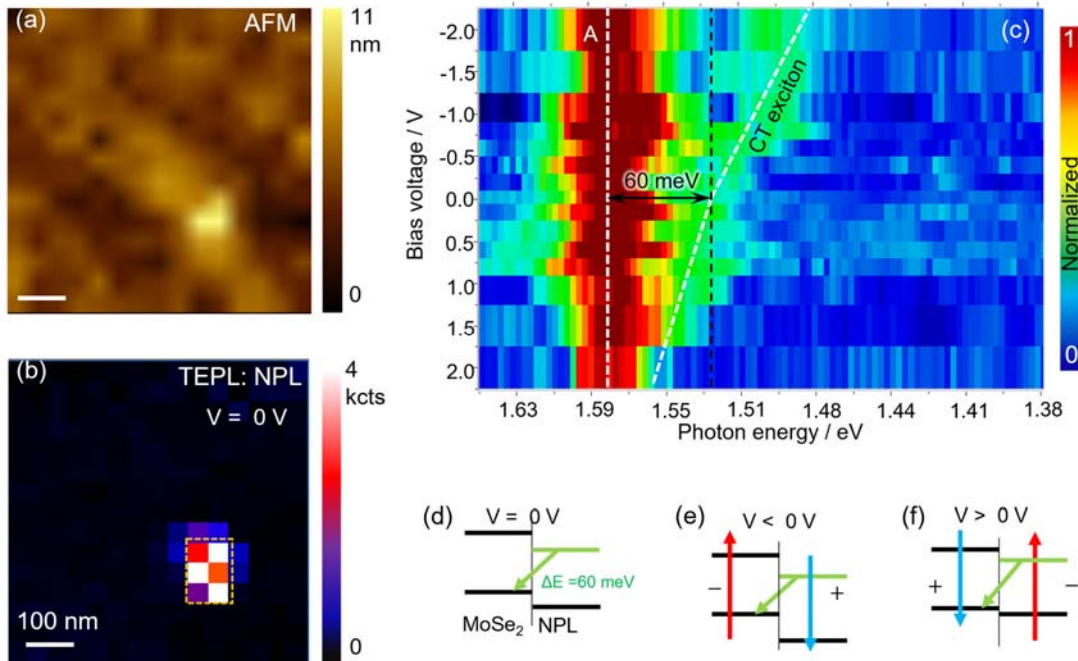143   NPLs exhibit strong (negligible) thickness dependent conduction band (CB) (valence band (VB))

Figure 3. *E*-field dependent tuning of CT excitons in MDH. (a) TEPL map of NPL and (b) corresponding AFM topography of the NPL/MoSe$_2$ system acquired simultaneously at 0V bias voltage. (c) Contour plot of *E*-field dependent TEPL spectra of the MDH system averaged over the rectangular area shown in (a). (d) – (f) Band alignment of the MDH at three different bias conditions.

144   tunability due to the small (large) conduction (valence) band offsets[26]. Hence, we can adjust the

145   band alignment of the studied MDH systems via shell thickness to tune the CT exciton energy

146   position. Fig. 2d displays NPL shell thickness dependent TEPL spectra of NPL/MoSe$_2$ MDH

147   systems. As the shell thickness increases (from 4.5 ML to 7.5 ML), the CT exciton energy can be

148   tuned up to 90 meV via tuning the band alignment. The process of band alignment tuning via NPL

149   shell thicknesses is schematically presented in Fig. 2e-g. Larger shell thickness results in a smaller

150   NPL bandgap, which moves the NPL CB minimum away (towards lower energy) from the

151   MoSe$_2$CB minimum. This results in a larger band offset and consequently smaller CT exciton

152   energies for thicker NPLs. In order to decouple CT excitons from strain and other local

153   heterogeneity induced shift we also conducted a comprehensive TEPL investigation of the

154   systems. Detailed studies of the local heterogeneities in the PL can be found in the supplementary

155   information section IV.

156   CT excitons have an out-of-plane dipole moment similar to the case of interlayer exciton

157   formation at a 2D/2D TMDC interface. This necessitated a study of the effect of out-of-plane E-

158   field on the evolution of CT excitons in the 2D/QD MDHs. For the E-field dependent TEPL study,

159   we used the same experimental configuration shown in Fig. 1a with a bias applied between the

160   tip and the substrate during measurements. Fig. 3a,b presents a NPL TEPL map and

161   corresponding AFM topography of the NPL/MoSe$_2$ MDH system acquired simultaneously at 0V

162   bias. For each bias voltage a complete TEPL map was acquired for the same region of interest and

163   an averaged TEPL spectra was created over the rectangle area marked in Fig. 3a. E-field

164   dependent TEPL spectra of the MDH for the spectral region between 1.65 to 1.38 eV are shown in

165   Fig. 3c. Evolution of NPL PL peak position as a function of bias voltage can be found in the

166   supplementary information section V. For a NPL PL peak of 1.85 eV we observed the CT exciton

167   at 60 meV below the MoSe$_2$ A exciton at 0V bias as schematically presented in the band diagram

168   of Fig. 3d. As the bias increases in the negative direction, the CT exciton drifted further away in

169   energy from the A exciton with a red shift of 120 meV observed at -2 V. The opposite trend was

170   observed in the positive bias direction, though at a slower rate. It was not possible to decouple

171   CT exciton from the A exciton peak above 1 V due to the close proximity and low single-to-noise

172   ratio. Fig. 3d-f are sketched to explain the CT exciton evolution under an out-of-plane E-field. At

173   0 V, we have the standard band alignment for which the CT exciton is observed. However, at

174   negative bias, the CB of MoSe$_2$ (NPL) increases (decreases) in energy. As a result, the CT exciton

175   moves away energetically from the A exciton to a lower energy. The opposite situation occurs at

176   a positive bias for which we observe the CT exciton move closer in energy to the A exciton of

177   MoSe$_2$. A similar behavior was recently reported for delocalized analogous CT excitons (IL

178   excitons) in a TMDC HB system[2,30].

179   A further proof of forming type II band alignment (prerequisite for CT exciton formation)

180   at NPL/TMDC (both $MoSe_2$ and WSe_2) heterointerfaces can be demonstrated by electrical

181   characterization. Fig. 4a,b present AFM and corresponding contact potential difference (CPD)

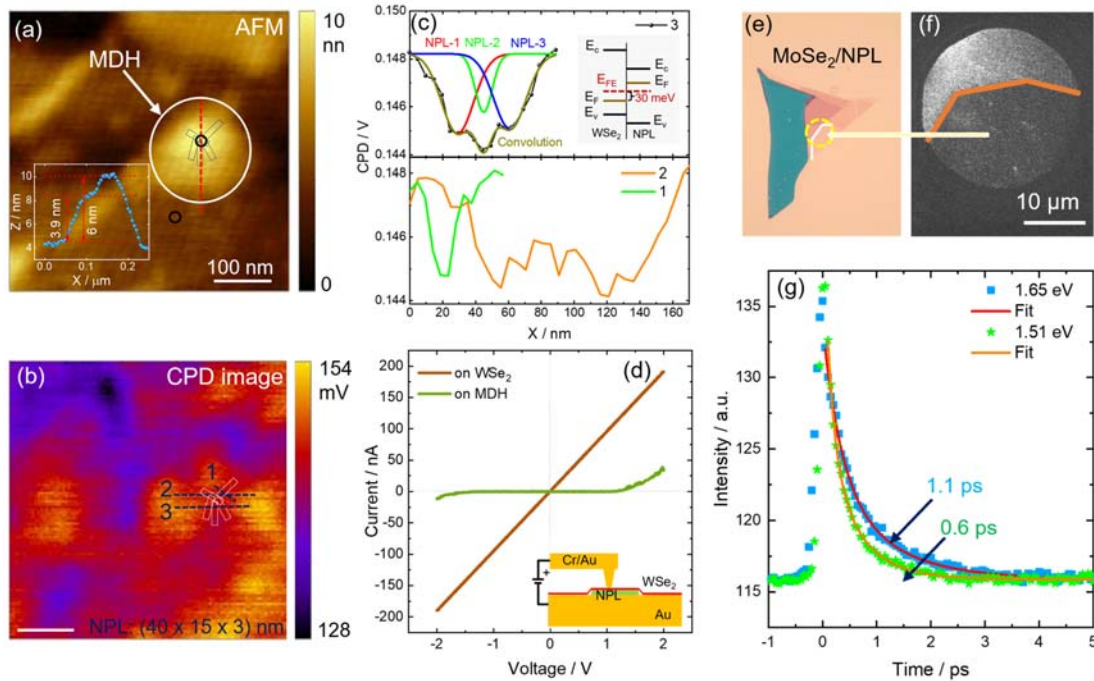182   images of a NPL/WSe_2 MDH system. The height profile of the MDH (inset of Fig. 4a) indicates a

Figure 4. Electrical and temporal characterization of MDH. (a), (b) AFM and corresponding CPD images of a WSe_2/NPL MDH system. The height profile of the MDH along the dotted red line is shown in the inset of (a). (c) Three separate CPD profiles extracted along the dashed lines in (b). The top panel is fitted with three Gaussians. Inset: schematic illustration of MDH band alignment at charge equilibrium condition. (d) Locally measured I – V curves on two different spots marked by black circles in (a) using conductive AFM. (e), (f) Optical and PEEM images of a MDH sample used for tr-PEEM measurements. (g) Time-resolved PEEM of the MDH acquired using two different excitation laser energies to determine the CT exciton dynamics. Decay curves were spatially-averaged over the dashed circle in (e).

183   cluster of NPLs with a possible pilling of two individual NPLs on top of each other since the

184   thickness of each NPL should be around 3 nm (see sample 1 in Table S1). The CPD image in Fig.

185   4b exhibits a more interesting and informative electronic picture of the MDH. Even though ML-

186   WSe_2 wraps the NPLs well and creates a single bulge in the topography, the CPD image shows

187   traces of several NPL/WSe$_2$ interfaces. To extract the Fermi level information at charge neutrality

188   conditions, we took three line profiles and plotted them in Fig. 4c. A gaussian fit to the line profile

189   1 provides a width of 13 nm (see supplementary information VI), which agrees well with the

190   width of a single NPL. Interestingly, CPD line profiles 2 and 3 show several dips of the same value

191   as line profile 1. Line profile 3 was fitted with three Gaussians: among them, the two outer ones

192   have slightly higher width, and the middle one has the same width as line profile 1. Using the

193   dimensions of the NPL, CPD line profiles and TEPL map (see Fig. SI-6), we sketched the MDH area

194   with five NPLs, as shown in Fig. 4a,b. To explain the interfacial charge transfer phenomenon a

195   schematic of the band diagram is plotted in the inset of Fig. 4c. Due to the Fermi level adjustment

196   via interfacial charge transfer, the surface potential of WSe$_2$ decreases by 30 - 40 mV at the MDH

197   interface, which is equivalent to a ~30 meV Fermi level rise at charge equilibrium conditions.

198   Fig. 4d displays the I – V curves measured locally using conductive-AFM on two different

199   spots of the sample marked by black circles in Fig. 4a. More I – V curves are presented in the

200   supplementary information section VI. Fig. 4d clearly demonstrates a rectification behavior for

201   the MDH. Whereas, on WSe$_2$ we observed a linear I-V response due to direct electrical tunnelling

202   or conduction through the ultra-thin layer of monolayer WSe$_2$.

203   Finally, we have used time-resolved photoemission electron microscopy (tr-PEEM) to

204   investigate the exciton dynamics of CT excitons in MDH. Fig. 4e,f show the optical and PEEM image

205   of the AOI region (outlined by circles). Exciton decay curves shown in Fig. 4g were derived from

206   spatially-averaged dynamics within the AOI region. The femtosecond pump- probe tr-PEEM

207   results of the MDH were acquired at two different pump excitation lasers: one at 1.65 eV covering

208   the MoSe$_2$ exciton region and the other at 1.51 eV which predominately excites CT exciton. To fit

209   the dynamics of the excitons both decay curves were fitted with bi-exponential functions with the

210   fit parameters listed in the table S2. From the fit, the MoSe$_2$ A exciton lifetime (excited by 1.65 eV)

211   is determined to be 1.1 ps. However, CT excitons generated at 1.51 eV show a shorter lifetime of

212   0.6 ps, which is in stark contrast to the lifetime of analogous ILXs in all 2D vdW heterostructures[2].

213   Indeed, the decay signal is the combination of both radiative and non-radiative recombination of

214   excitons. At elevated temperature (tr-PEEM measurements were performed at RT) non-radiative

215   decay through Augur scattering or charge trapping at defects dominates, which occurs on a faster

216   time scale than radiative recombination [31,32]. Since $CdSe/Cd_xSZn_{1-x}S$ core/shell nanocrystals are

217   known for surface defects/trap states[33], the probability of non-radiative recombination of CT

218   excitons is higher at the $MoSe_2$/NPL interface than for the $MoSe_2$ A exciton in the 2D plane. A

219   similar behavior was also observed by Bouleshba et al[34] at a WS_2/QD heterointerface. Hence, we

220   observe a shorter CT exciton life time relative to the $MoSe_2$ A exciton in the present work.

Conclusion

222   In summary, we report the formation of CT excitons in a MDH containing 2D TMDCs and

223   quasi-2D NPLs. We adopted TEPL to spatially resolve CT exciton formation sites at the single

224   NPL/TMDC interface. To the best of our knowledge, this is the primary observation of such

225   localized CT excitonic phenomena in a MDH at RT. To confirm the origin of CT excitons, we

226   adopted a systematic approach via changing both the TMDC material and the shell thickness of

227   NPLs. Both approaches give a wide range of tunability of the CT exciton energy, up to 100 meV.

228   Out-of-plane *E*-field dependent TEPL also provides an excellent knob to tune the CT exciton with

229   a tunable range of 120 meV. Our work opens a new pathway for manipulating excited states at

230   mixed-dimensional interfaces, which offers great promise both for fundamental studies and

231   optoelectronic applications, opening doors to electrical control of colloidal quantum materials via

232   electronic heterointerfaces with 2D materials.

Methods

234   **Synthesis of rectangular CdSe nanoplatelets:** The cadmium myristate precursor is

235   prepared by following the literature[35]. Colloidal, rectangular CdSe nanoplatelets with a thickness

236   of 4.5 monolayers are synthesized following the literature[36] with slight modifications[37,38] that are

237   described in detail in the supplementary information section SI-I.

238   **Synthesis of square-like CdSe nanoplatelets:** Colloidal, square-like CdSe nanoplatelets

239   with a thickness of 4.5 monolayers are synthesized by following prior literature[39] with slight

240   modifications that are described in detail in the supplementary information section SI-I.

241   **Growth of $Cd_xZnS_{1-x}S$ shell:** Cadmium $(Cd(Ol)_2)$ and zinc oleate $(Zn(Ol)_2)$ are synthesized

242   according to the literature[39,40]. The growth of a $Cd_xZnS_{1-x}S$ shell with increasing thickness on CdSe

243   nanoplatelets is performed by following the literature[39] with minor modifications that are

244   described in detail in the supplementary information section SI-I.

245   **MDH device preparation**: Both ultra-smooth Au and 5 nm Al_2O_3 coated Au substrates

246   were used for the sample preparation. Al_2O_3 films were deposited on Au using ALD (Cambridge

247   Nanotech) via chemical reaction of metal organic precursor, Trimethylaluminium with water

248   vapors in each cycle at 150 °C, which typically yielded a deposition rate of 0.9 Å/cycle. To prepare

249   the ultra-smooth Au surface, ~100 nm of Au was first deposited on Si with native oxide (without

250   any adhesion layer) using the thermal evaporation technique. After that, the buried ultra-smooth

251   Au face was stripped-off using an epoxy resin supported Si substrate, which were then used as

252   the active substrates for the MDH devices.

253   To prepare the devices, a very dilute solution of NPL (0.001 mg/mL) was first spin coated

254   at a speed of 3000 rpm for 60 s on the Au (or Al_2O_3/Au) substrate. After that, monolayer TMDCs

255   were transferred on top of NPLs/Au via deterministic dry transfer method. All the sample were

256   then annealed in an Ar/H2 atmosphere for 2 h at 120 °C.

257   **Micro-PL characterization**: A Horiba LabRam HR evolution equipped with 633 nm

258   excitation laser and an electron multiplying charge coupled detector was used for micro-PL

259   measurements. PL measurements were carried out using 100 l/mm grating and 100 μW power

260   (measured at the sample surface) focused on the sample surface via a 100 x, 0.9 NA objective. PL

261   maps were acquired using 500 x 500 nm step size, which is well above the diffraction limit at this

262   wavelength. Signal acquisition time was set at 0.2 s during the mapping.

263 **TEPL characterization**: TEPL measurements were carried out using a Horiba NanoRaman

264 platform consisting of the same Horiba LabRam HR evolution coupled with an AIST-NT AFM.

265 Commercially available Au TERS tips were used for the measurements under *p*-polarized 633 nm

266 excitation in side illumination/collection geometry at an angle of 65° from the normal to the

267 sample surface. The laser power was kept at 20 μW focused onto the tip apex using a 100x 0.7 NA

268 objective and the acquisition time was set at 0.2 s. Both the near-field PL spectra and far-field

269 background were collected for each pixel one after another during TEPL map acquisition via a

270 hybrid tip operating mode. Far-field background was measured during the tip normal oscillation

271 period in non-contact mode and the near-field signal was collected by bringing the tip in contact

272 to the sample. Both measuring steps were repeated one after another at each pixel to collect

273 complete near-field plus far-field and far-field only PL maps of the sample. A step size of 20 x 20

274 nm was used for the all the TEPL mapping except for the *E*-field dependent study, for which a 40

275 x 40 nm step size was used. For the *E*-field dependent study, a bias was applied to the tip and kept

276 constant during map acquisition.

277 **I – V characterization**: I – V characterization of the MDH were performed using conductive

278 AFM and commercially available Cr/Au probes.

279 **Time-resolved PEEM**: The PEEM experiments were performed using a commercial

280 titanium-sapphire oscillator (Griffin-10, KM Labs) producing sub-20 fs pulses centered at 780 nm

281 at a 90 MHz repetition rate. A slit within the laser cavity is used for fundamental wavelength (740-

282 840 nm range) and bandwidth tuning. Approximately 30% of the pulse is split to produce the

283 second harmonic probe pulse in a 200 μm thick BBO crystal. The resulting blue light is

284 recompressed in a CaF_2 prism pair to yield second harmonic pulses of less than 50 fs. A variable

285 delay line controls the relative timing between the red (~800 nm) pump and blue (~400 nm)

286 probe pulses. *P*-polarized laser pulses are recombined on a dichroic beam splitter and directed

287 collinearly onto the PEEM sample at a 75° angle of incidence with respect to the surface normal.

288 The spot sizes of the separate beams are adjusted such that typically the red pulse spot size is

289   roughly 50% smaller than the blue pulse spot size at the sample position. A typical spot size for

290   the red laser is 40 x 120 microns at the sample. PEEM images are collected as a function of probe

291   delay time, yielding time resolved movies of photoelectron emission dynamics. Cross-correlation

292   of the red and blue pulses yields time resolution of less than 80 fs for all wavelengths pairs used

293   in this study. Typically, 50-100 mW of ~800 nm power is used in combination with 3-6 mW of

294   ~400 nm laser light for experiments described herein.

295   **Author Contribution**

296   M.R. and D.J. conceived the idea and designed the research. M.R. implemented the project via

297   sample fabrication, performing far/near-field-PL, CPD and, c-AFM measurements and analyzing

298   and interpreting the data. E.M. and Z.J. synthesized the nanoplates under the supervision of C.B.M.

299   A.G.J and B.T.O-C. conducted time-resolved exciton lifetime measurements under the supervision

300   of P.Z.K. S.S. and K.J. contributed to the sample fabrication. G.K. contributed to far-field PL

301   measurements. D.R. performed TEM of nanoplates. M.R. and D.J. wrote the manuscript with inputs

302   from all coauthors.

References

1. Alexandrou, A. *et al.* Electric-field effects on exciton lifetimes in symmetric coupled GaAs/Al0.3Ga0.7As double quantum wells. *Phys. Rev. B* **42**, 9225 (1990).

2. Rivera, P. *et al.* Observation of long-lived interlayer excitons in monolayer MoSe2–WSe2 heterostructures. *Nat. Commun. 2015 61* **6**, 1–6 (2015).

3. Wang, Z. *et al.* Evidence of high-temperature exciton condensation in two-dimensional atomic double layers. *Nat. 2019 5747776* **574**, 76–80 (2019).

4. Paik, E. Y. *et al.* Interlayer exciton laser of extended spatial coherence in atomically thin heterostructures. *Nat. 2019 5767785* **576**, 80–84 (2019).

5. Islam, M. N. *et al.* Electroabsorption in GaAs/AlGaAs coupled quantum well waveguides. *Appl. Phys. Lett.* **50**, 1098 (1998).

6. Steiner, T. W., Wolford, D. J., Kuech, T. F. & Jaros, M. Auger decay of X-point excitons in a type II GaAs/AlGaAs superlattice. *Superlattices Microstruct.* **4**, 227–232 (1988).

7. Jiang, Y., Chen, S., Zheng, W., Zheng, B. & Pan, A. Interlayer exciton formation, relaxation, and transport in TMD van der Waals heterostructures. *Light Sci. Appl.* **10**, 1–29 (2021).

8. Rivera, P. *et al.* Interlayer valley excitons in heterobilayers of transition metal dichalcogenides. *Nat. Nanotechnol.* **13**, 1004–1015 (2018).

9. Mak, K. F. & Shan, J. Opportunities and challenges of interlayer exciton control and manipulation. *Nat. Nanotechnol.* **13**, 974–976 (2018).

339   10.   Ruiz-Tijerina, D. A. & Fal'Ko, V. I. Interlayer hybridization and moiré superlattice

340   minibands for electrons and excitons in heterobilayers of transition-metal

341   dichalcogenides. *Phys. Rev. B* **99**, 30–32 (2019).

342   11.   Brem, S., Linderälv, C., Erhart, P. & Malic, E. Tunable Phases of Moiré Excitons in van der

343   Waals Heterostructures. *Nano Lett.* **20**, 8534–8540 (2020).

344   12.   Interlayer excitons and how to trap them. *Nat. Mater. 2020 196* **19**, 579–579 (2020).

345   13.   Yu, H., Liu, G. Bin, Tang, J., Xu, X. & Yao, W. Moiré excitons: From programmable quantum

346   emitter arrays to spin-orbit–coupled artificial lattices. *Sci. Adv.* **3**, 1–8 (2017).

347   14.   Seyler, K. L. *et al.* Signatures of moiré-trapped valley excitons in MoSe2/WSe2

348   heterobilayers. *Nature* **567**, 66–70 (2019).

349   15.   Li, W., Lu, X., Dubey, S., Devenica, L. & Srivastava, A. Dipolar interactions between

350   localized interlayer excitons in van der Waals heterostructures. *Nat. Mater.* **19**, 624–629

351   (2020).

352   16.   Jadwiszczak, J. *et al.* Mixed-Dimensional 1D/2D van der Waals Heterojunction Diodes and

353   Transistors in the Atomic Limit. *ACS Nano* **16**, 1639–1648 (2022).

354   17.   Mouafo, L. D. N. *et al.* 0D/2D Heterostructures Vertical Single Electron Transistor. *Adv.*

355   *Funct. Mater.* **31**, 2008255 (2021).

356   18.   Zereshki, P. *et al.* Observation of charge transfer in mixed-dimensional heterostructures

357   formed by transition metal dichalcogenide monolayers and PbS quantum dots. *Phys. Rev.*

358   *B* **100**, 1–8 (2019).

359   19.   Xiao, J. *et al.* Type-II Interface Band Alignment in the vdW PbI2-MoSe2Heterostructure.

360   *ACS Appl. Mater. Interfaces* **12**, 32099–32105 (2020).

361   20.   Jariwala, D., Marks, T. J. & Hersam, M. C. Mixed-dimensional van der Waals

362   heterostructures. *Nat. Mater.* **16**, 170–181 (2017).

363   21.   Zhu, X. *et al.* Charge Transfer Excitons at van der Waals Interfaces. *J. Am. Chem. Soc.* **137**,

364   8313–8320 (2015).

365   22.   Goodman, A. J., Dahod, N. S. & Tisdale, W. A. Ultrafast Charge Transfer at a Quantum

366   Dot/2D Materials Interface Probed by Second Harmonic Generation. *J. Phys. Chem. Lett.* **9**,

367   4227–4232 (2018).

368   23.   Zhang, K. *et al.* Electrical control of spatial resolution in mixed-dimensional

369   heterostructured photodetectors. *Proc. Natl. Acad. Sci. U. S. A.* **116**, 6586–6593 (2019).

370   24.   Burdanova, M. G. *et al.* Intertube Excitonic Coupling in Nanotube Van der Waals

371   Heterostructures. *Adv. Funct. Mater.* **32**, 2104969 (2022).

372   25.   Ithurria, S. *et al.* Colloidal nanoplatelets with two-dimensional electronic structure. *Nat.*

373   *Mater. 2011 1012* **10**, 936–941 (2011).

374   26.   Eshet, H., Grünwald, M. & Rabani, E. The electronic structure of CdSe/CdS Core/shell

375   seeded nanorods: Type-I or quasi-type-II? *Nano Lett.* **13**, 5880–5885 (2013).

376   27.   Gong, C. *et al.* Band alignment of two-dimensional transition metal dichalcogenides:

377   Application in tunnel field effect transistors. *Appl. Phys. Lett.* **103**, 053513 (2013).

378   28.   Rahaman, M. *et al.* Observation of Room-Temperature Dark Exciton Emission in

379   Nanopatch-Decorated Monolayer WSe2 on Metal Substrate. *Adv. Opt. Mater.* (2021)

380   doi:10.1002/adom.202101801.

381   29.   Park, K. D., Jiang, T., Clark, G., Xu, X. & Raschke, M. B. Radiative control of dark excitons at

382   room temperature by nano-optical antenna-tip Purcell effect. *Nat. Nanotechnol.* **13**, 59–

383   64 (2018).

384   30.   Ciarrocchi, A. *et al.* Polarization switching and electrical control of interlayer excitons in

385   two-dimensional van der Waals heterostructures. *Nat. Photonics* **13**, 131–136 (2019).

386   31.   Javaux, C. *et al.* Thermal activation of non-radiative Auger recombination in charged

387   colloidal nanocrystals. *Nat. Nanotechnol. 2013 83* **8**, 206–212 (2013).

388   32.   Moody, G., Schaibley, J. & Xu, X. Exciton dynamics in monolayer transition metal

389   dichalcogenides [Invited]. *JOSA B, Vol. 33, Issue 7, pp. C39-C49* **33**, C39–C49 (2016).

390   33.   Minotto, A. *et al.* Role of core-shell interfaces on exciton recombination in CdSe-CdxZn1-

391   xS quantum dots. *J. Phys. Chem. C* **118**, 24117–24126 (2014).

392   34.   Boulesbaa, A. *et al.* Ultrafast Charge Transfer and Hybrid Exciton Formation in 2D/0D

393   Heterostructures. *J. Am. Chem. Soc.* **138**, 14713–14719 (2016).

394   35.   Carion, O., Mahler, B., Pons, T. & Dubertret, B. Synthesis, encapsulation, purification and

395   coupling of single quantum dots in phospholipid micelles for their use in cellular and in

396   vivo imaging. *Nat. Protoc. 2007 210* **2**, 2383–2390 (2007).

397   36.   She, C. *et al.* Red, Yellow, Green, and Blue Amplified Spontaneous Emission and Lasing

398   Using Colloidal CdSe Nanoplatelets. *ACS Nano* **9**, 9475–9485 (2015).

399   37.   Marino, E. Assembling nanocrystal superstructures. (Universiteit van Amsterdam, 2019).

400   38.   Marino, E. *et al.* Repairing Nanoparticle Surface Defects. *Angew. Chemie Int. Ed.* **56**,

401   13795–13799 (2017).

402   39.   Rossinelli, A. A. *et al.* Compositional Grading for Efficient and Narrowband Emission in

403   CdSe-Based Core/Shell Nanoplatelets. *Chem. Mater.* **31**, 9567–9578 (2019).

404   40.   Hendricks, M. P., Campos, M. P., Cleveland, G. T., Plante, I. J. La & Owen, J. S. A Tunable

405   library of substituted thiourea precursors to metal sulfide nanocrystals. *Science (80-.).*

406   **348**, 1226–1230 (2015).

407